# RADIATION SOURCES AND THEIR APPLICATION FOR BEAM PROFILE DIAGNOSTICS

G. Kube
DESY, Hamburg, Germany

*Abstract*

Radiation generated by high-energy particle beams is widely used for beam diagnostic purposes. Depending on the mechanism of radiation generation, the emitted wavelength range extends from the THz up to the X-ray region, thus allowing to measure beam profiles in the longitudinal and the transverse plane over a wide range. In this talk, basic considerations for radiation based profile measurements will be discussed with special emphasis on the mechanism of radiation generation and the impact on beam diagnostic measurements.

## INTRODUCTION

Beam monitors probing the particle electromagnetic field are widely used in accelerator physics. The majority of them is sensitive to the particle near field, i.e. the field which is directly bound to the charged particle, and a usable signal is derived from the interaction of this field with the environment. Examples of this kind of monitors are beam position and beam current monitors. In an other type of monitors, information about the beam properties is generated from the fields which are separated from the charged particle itself. These freely propagating fields can be measured at large distances from the particle as radiation in a wide spectral range, even outside of the accelerator tunnel. Depending on the separation mechanism of the electromagnetic field, the process of radiation generation is named in a different way. Examples considered in the following are synchrotron radiation, transition radiation, diffraction radiation, parametric X–ray radiation, and Smith–Purcell radiation. A comprehensive overview of the radiation generation by ultra–relativistic particles can be found for example in the textbooks [1]– [4], actual topics in radiation physics are discussed at the RREPS conference series [5] or at the conference series *Charged and Neutral Particles Channeling Phenomena*.

All radiation mechanisms mentioned before are either widely applied or investigated in view of an applicability in the field of particle beam diagnostics in different ways. A vast number of information can be extracted from the radiation field, as for example beam energy, energy width and beam divergence, but in the following only beam profile measurements will be considered. In this context, the transverse beam profile diagnostics based on imaging with visible radiation is widespread, the focus will be on their description and the applied concepts (see also Ref. [6]). Besides beam imaging techniques, a measurement of the angular distribution can also be gathered to gain information about the transverse beam profile. Finally, coherent radiation diagnostics is a technique to determine both shape and length of a charged particle bunch by spectral investigation of the coherently emitted radiation.

Starting from imaging with classical light and a discussion about resolution, the radiation generation from ultra–relativistic particles is described in terms of the separation of the pseudo- or virtual photon field associated with the charged particle (Weizsäcker–Williams approximation [7,8]). In this picture, the various radiation processes appear as different ways to separate the virtual photons from the particle, and the formalism of classical imaging can simply be applied to the separated field. Examples are given for particle beam imaging, and the concept of beam size determination from the angular distribution is presented for different radiation sources. Finally, bunch length diagnostics based on coherent Smith–Purcell radiation is presented as an example.

## IMAGE FORMATION AND RESOLUTION

In the case of particle diagnostics, the object from which the size has to be determined, i.e. the particle bunch, is not directly accessible because it is moving in a vacuum beam pipe in the accelerator tunnel. In this situation, radiation based diagnostics in general and imaging in particular helps to generate a replica of the object in a more comfortable environment, and the replica size (image) is adjusted to size of measuring device (CCD) with the help of an optical system (lenses). In the subsequent discussion about imaging, only aberration–free optical systems will be considered. Nevertheless, from classical optics it is known that even for imaging with a perfect lens, the image of a point source will never result in a point image because the uncertainty relation imposes a fundamental limit $\Delta x = \lambda/(2\sin\theta)$ with $\Delta x$ the uncertainty in the location of the emission point, $\lambda$ the wavelength of observation, and $\sin\theta$ the acceptance angle (numerical aperture) of the imaging lens. To be more precise, the point source image is the result of plane wave diffraction at a circular aperture (lens), and the intensity distribution in the image plane is described by the well known Airy disk (see eg. [9] or textbooks about classical optics). The resolution is usually expressed as the first minimum of the Airy disk

$$\Delta x = 0.61\frac{M\lambda}{\sin\theta} \qquad (1)$$

with the magnification factor $M$ of the optical setup.

A deeper discussion of the resolution requires some basic knowledge of the image formation process. For this purpose a simple optical setup is considered as shown in Fig. 1. The common procedure is to calculate the intensity distribution of a point source in the image plane which is proportional to

ISBN 978-3-95450-141-0

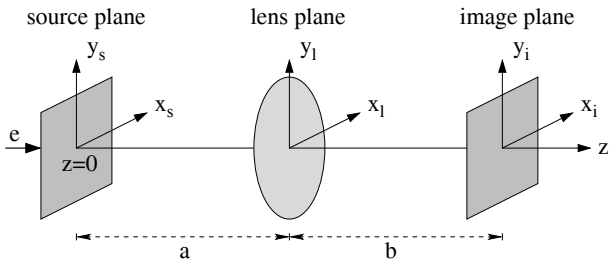


Figure 1: Scheme of the optical setup. Source and image planes are located at distances $a, b$ from the perfect lens, the magnification of the system is $M = b/a$.

the absolute square of the electric fields in this plane. This point source image is referred to as Point Spread Function (PSF), and the PSF is characterizing the optical system properties. In analogy to the PSF definition in classical optics, the image generated in a radiation process from a single particle will be called PSF throughout the rest of this paper, being aware that in this case the PSF is not only determined by the optical system properties, but also by the particle properties (beam energy) which influence the radiation characteristics, e.g. the opening angle. The image of an extended object is obtained by a two–dimensional convolution of the source distribution with the PSF, and the resolution is the difference between source and image distribution for a magnification of $M = 1$.

In order to calculate the PSF, the electric field from the source plane has to be propagated through the optical system to the image plane, taking into account the interaction of each optical element. In the simple setup shown in Fig. 1, the source field distribution has to be propagated from the source plane to the lens entrance plane, from there to the lens exit plane, and then to the image plane. The propagation is performed in frame of scalar diffraction theory in Fresnel approximation, i.e. up to the quadratic phase term. With the target located at $z = 0$ the propagation from the source plane $S_{src}$ to the lens input in a distance $a$ is described by

$$E^{l_i}_{x_l,y_l}(\vec{r_l},\omega) = -i\,\frac{e^{ika}}{\lambda a}\, e^{i\frac{k}{2a}(x_l^2+y_l^2)} \ldots \quad (2)$$
$$\times \int_{S_{src}} \mathrm{d}^2 S_{src}\; E^{s}_{x_s,y_s}(\vec{r_s},\omega)\; e^{i\frac{k}{2a}(x_s^2+y_s^2)}\; e^{-ik\frac{x_s x_l + y_s y_l}{a}}$$

see for example Ref. [10]. The integration has to be carried out over the source plane $\Sigma_s$, and special care has to be taken to the integration limits. They may either be defined by the target dimensions or by the radiation field and will be annotated later in more detail. In the far field or Fraunhofer approximation $\frac{k}{2}(x_s^2 + y_s^2)_{max} \ll a$, the corresponding exponential in the integration can be omitted, and in this limit the field in the lens plane is proportional to the two–dimensional Fourier transformation of the source field distribution, c.f. Eq. (2). In the next step the resulting field Eq. (2) is propagated through the lens. In thin lens approximation the effect of the lens is described by introducing an additional quadratic phase shift [10], and the fields at the lens output are given by

$$E^{l_o}_{x_l,y_l}(\vec{r_l},\omega) = E^{l_i}_{x_l,y_l}(\vec{r_l},\omega)\; e^{-i\frac{k}{2f}(x_l^2+y_l^2)} \quad (3)$$

with $f$ the focal length of the lens and $\frac{1}{f} = \frac{1}{a} + \frac{1}{b}$ the condition for imaging. In the next step, the field has to be propagated from the lens output to the image plane similar to Eq. (2), and finally the intensity distribution in the image plane

$$\frac{\mathrm{d}^2 W}{\mathrm{d}\omega \mathrm{d}\Omega} = \frac{c}{4\pi^2}\,(|E^i_{x_i}|^2 + |E^i_{y_i}|^2)\,. \quad (4)$$

has to be calculated. If the source field distribution is from a point source or from radiation of a single charged particle, this intensity distribution is representing the PSF.

Based on the concept of Fourier optics and the image generation

$$\text{Image} = \text{PSF} \otimes \text{Object} + \text{Noise}\,, \quad (5)$$

the process of imaging can be described in the frame of system theory, see also Fig. 2. In standard system theory the signals are one–dimensional, treated in the time/frequency domain, and system analysis is performed with a delta pulse. In the case of imaging one is dealing with two–dimensional signals (space coordinates), treated in the space/spatial frequency domain (line pairs per mm), and system analysis is performed with a point source.

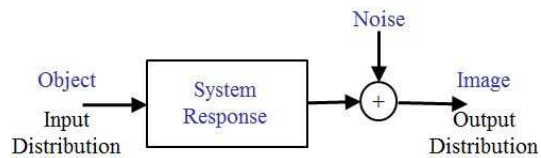


Figure 2: System approach to imaging. The system response is described by the PSF which acts on the input distribution to produce the output.

## RADIATION GENERATION

To apply standard optical imaging techniques, the information about the particle beam charge distribution has to be converted in an optical intensity distribution which can be recorded by camera. In the selection of this conversion process, care has to be taken that (i) any resolution broadening introduced by the basic underlying physical process has to be small (i.e. the PSF of the physical process corresponding to the single particle resolution function should not dominate the total spatial resolution), and that (ii) the conversion process should be linear to avoid any deformation of the intensity distribution. There exist two principle possibilities for this conversion process, either to exploit the interaction of the beam particles with matter (used e.g. for scintillation screens or residual gas luminescent monitors), or the particle electromagnetic field has to be separated from the beam to be detected in the far field as radiation.



ISBN 978-3-95450-141-0

While scintillators are widely used in particle beam diagnostics at hadron and electron accelerators [11], in the following only radiation based beam profile monitors will be considered. Therefore the process of radiation generation is shortly explained in this section in the frame of virtual photons: Considering an ultra–relativistic particle with an electric field which is relativistic contracted (i.e. mainly transversal), the degree of contraction is described by the field opening angle $1/\gamma$ with $\gamma = E/m_0c^2$ the Lorentz factor. Hadrons have a comparatively large rest mass and $\gamma$ is much smaller than the one for electrons. Therefore radiation based monitors are the exception rather than the rule at hadron accelerators, and in the following only ultra–relativistic electron or positron beams are considered.

In the limiting case $\gamma \to \infty$ the field would be completely transversal and correspond to a plane wave (classical description of a photon). This situation occurs either by considering a particle with zero rest mass (i.e. a photon), or in the limiting case if the beam energy is increased into the ultra–relativistic regime. Due to the similarity between a real photon and the field of an ultra–relativistic particle, the action of this particle is described by so called virtual or pseudo photons. However, to measure radiation in the far field the virtual photon field bound to the beam particle has to be separated from the particle. In case of a circular accelerator this is achieved by a force acting on the charged particle which is caused by the magnetic field of accelerator (bending) magnets, and the resulting radiation is called *synchrotron radiation*. In case of a linear accelerator there is (per definition) no particle bending, but the separation can be achieved by acting on the virtual photons itself via structures that diffract the particle electromagnetic field away from the particle. The analogy between real and virtual photons can be exploited for better understanding: Real photons can be refracted resp. reflected at a surface, and the same holds for virtual photons. In this case the radiation is named *Forward/Backward Transition Radiation*. In classical optics the effect of edge diffraction is known, in the case of virtual photons the radiation effect is called *Diffraction Radiation*. Real photons can be diffracted at a grating, the same hold for virtual photons and the effect is called *Smith–Purcell Radiation*. Finally, high–energetic real photons (X–rays) are diffracted at a 3D structure of a crystal, and if a charged particle beam traverses such crystal *Parametric–X Radiation* is emitted.

## SYNCHROTRON RADIATION

Synchrotron radiation (SR) is a versatile tool for beam profile measurements due to its non–destructive nature. While in principle SR from insertion devices or bending magnets can be utilized, in reality most accelerators use bending magnet radiation based profile monitoring because of space limitations. Due to the relativistic energy of the particles, the generated light has superior properties [12]: The process of radiation generation is non–invasive and the radiation spectrum is continuous from infrared up to X-rays. As consequence the photon energy can be freely chosen according to the monitoring problem. Typically the spectrum is characterized by the critical energy $\hbar\omega_c = \frac{3}{2}\hbar c\frac{\gamma^3}{\rho}$ with $\gamma$ the Lorentz factor and $\rho$ the dipole bending radius. The natural divergence of the radiation which depends on the polarization state is very small with a vertical opening angle of about $1/\gamma$ in case of horizontal ($\sigma-$) polarization.

In order to apply the formalism of image formation to the case of SR based diagnostics, the source field has to be determined. According to the geometry depicted in Fig. 3, the field of a moving charge is described by the Liénard–Wiechert potentials. The common way found in most textbooks about electrodynamics is to deduce the fields in the time domain

$$\vec{E}(t) = -e\left(\frac{(1-\beta^2)(\hat{n}-\vec{\beta})}{R^2(1-\hat{n}\cdot\vec{\beta})^3} + \frac{\hat{n}\times[(\hat{n}-\vec{\beta})\times\dot{\vec{\beta}}]}{cR(1-\hat{n}\cdot\vec{\beta})^3}\right)_\tau$$
$$\vec{H}(t) = (\vec{n}\times\vec{E})_\tau \ . \qquad (6)$$

which have to be evaluated at the retarded time $\tau = t - R(\tau)/c$. In the far field approximation, the first term in the sum which does not depend on the acceleration (the so called velocity term) is usually omitted because it scales quadratically with the distance to the observer. To get rid of the retarded time, the fields are transformed in the Fourier domain, and if the special case of a particle motion on a circular orbit is considered, the standard formulas for the SR fields are derived [12]. SR imaging investigations based on this field description are presented in Ref. [13].

However, the radiation fields derived in this way are only approximative because of the far field approximation. Furthermore, in this approach the emission is considered to originate from a single point, additional resolution broadening effects as depth–of–field and orbit curvature have to be introduced additionally [14, 15].

In the approach of Ref. [16] these contributions are included from the beginning. Starting point are again the Liénard–Wiechert potentials, but this time the potentials are Fourier transformed and the fields are derived in the

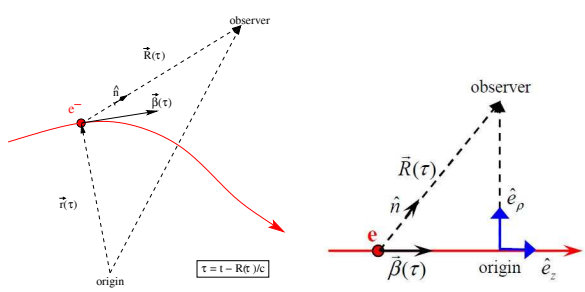


Figure 3: Geometry for the description of the Liénard–Wiechert fields for a particle in arbitrary (left) and linear (right) motion.

ISBN 978-3-95450-141-0

frequency domain, resulting in an integral equation

$$\vec{E}(\omega) = -\frac{i\omega e}{c}\int_{-\infty}^{+\infty} \mathrm{d}\tau \left[\frac{\vec{\beta}-\hat{n}}{R(\tau)} - \frac{ic}{\omega}\frac{\hat{n}}{R^2(\tau)}\right] e^{i\omega(\tau+\frac{R(\tau)}{c})} . \tag{7}$$

The integration can be performed numerically with high accuracy using e.g. numerical near field calculations [16] in order to study resolution broadening effects. Codes like SRW [17] or SPECTRA [18] are freely available allowing computations preserving all phase terms that are necessary for further propagation of the radiation through optical components. In SRW, even propagation is implemented in the frame of scalar diffraction theory applying the methods of Fourier optics. Besides the numerical near field calculation, there exist also analytical approaches in which the disturbed wave front is characterized by an additional phase factor such that orbit curvature and depth–of–field influence can directly be included in the radiation field description [19–21].

A review of SR based diagnostics for transverse profile measurements is given in Ref. [22], therefore only some basic considerations for modern $3^{rd}$ generation light sources are discussed in the following. For these machines with natural emittances in the order of 1 - 5 nm.rad and an emittance coupling of 1 %, the task is to resolve few micrometer beam sizes. For PETRA-III at DESY (Hamburg, Germany) for example, the beam sizes which have to be measured amount $\sigma_x = 40\,\mu\mathrm{m}$ and $\sigma_y = 20\,\mu\mathrm{m}$. Recalling that the fundamental resolution limit depends on the acceptance angle $\vartheta$, and that the limit in the acceptance is not dictated by the lens diameter but by the extremely small SR emission angle in vertical direction (with $\vartheta_{acc} = 1.7$ mrad for PETRA-III), observation in the visible spectral region ($\lambda = 500$ nm) would result in a vertical resolution of about 145 µm according to the uncertainty principle which is much larger than the beam size which has to be measured. Beam profile measurements based on visible SR are therefore fully diffraction limited at modern light sources.

The most straightforward way to overcome this limitation is imaging at smaller wavelength in the VUV, soft or even hard X–ray region. In this case the discussion about a monitor concept is reduced to the question about the appropriate imaging optics. In the case of imaging with focusing optics either reflective (Kirkpatrick–Baez mirror), diffractive (Fresnel zone plates) or refractive (compound refractive lens) optics can be used, and all these concepts are applied at different accelerator laboratories, see Ref. [22]. In the case of a non–focusing optics, the most prevalent device is the X–ray pinhole camera (see e.g. Ref. [23]). Besides the imaging schemes, other techniques are applied as the SR interferometer exploiting the spatial coherence of the radiation [24], the $\pi$–polarization imaging as a special case of PSF dominated imaging [25], and the coded aperture technique [26].

## CONSTANT LINEAR MOTION

For the discussion about radiation based imaging techniques in linear accelerators, the electromagnetic field of a point particle in constant linear motion is considered as it is the case for an electron in a drift space. Again the particle field is given by the Liénard–Wiechert field in Eq. (6), however in this situation it is the second term in the sum (acceleration term) which vanishes because there is no acceleration per definition. Because of the rotational symmetry it is convenient to describe the geometry in the cylindrical coordinate system as shown in Fig. 3, right. In this system, the electric field can be expressed as [1]

$$\vec{E}(\rho,z,\omega) = \frac{e\alpha}{\pi v}\, e^{i\frac{\omega}{v}z}\left(\mathrm{K}_1(\alpha\rho)\,\hat{e}_\rho - \frac{i}{\gamma}\,\mathrm{K}_0(\alpha\rho)\,\hat{e}_z\right) \quad \text{with} \quad \alpha = \frac{2\pi}{\lambda\beta\gamma} \tag{8}$$

and $\mathrm{K}_0$, $\mathrm{K}_1$ the modified Bessel functions. While $\mathrm{K}_0$ is already smaller than $\mathrm{K}_1$, according to Eq. (8) in the ultra–relativistic limit $\gamma \to \infty$ the contribution from the longitudinal component can be completely neglected and the particle field exhibits the typical pancake structure. It is this field which is associated with the pseudo photons in order to describe the different radiation generation mechanisms.

With increasing distance $\rho$ from the beam orbit, the field shrinks following the $\mathrm{K}_1$ dependency. It is convenient to assign a value to the radial field extension $\rho_{ext}$ by setting the argument of the Bessel function equal one, i.e.

$$\rho_{ext} = \frac{\lambda\beta\gamma}{2\pi} \approx \gamma\lambda . \tag{9}$$

In a descriptive way the virtual photon field is interpreted as a radial field disc with the radius $\rho_{ext}$. The angular distribution of the virtual photon field is given by

$$\frac{\mathrm{d}^2W}{\mathrm{d}\omega\mathrm{d}\Omega} = \frac{e^2}{\pi^2 c}\frac{\theta^2}{(\gamma^{-2}+\theta^2)^2} . \tag{10}$$

These photons associated to the charged particle beam possess therefore a characteristic double lobe structure with a central minimum, and it is this structure which is imprinted to the real photons (radiation) when the field is separated from the beam.

The pseudo photon approach presented here in a descriptive way implies a simplification in the sense that only the transverse field components are considered. In Refs. [27,28] the contribution of the longitudinal component was taken additionally into account, allowing an extension of the theory to low particle beam energies and arbitrary inclination angles. This was done either by developing a vector electromagnetic theory for transition and diffraction radiation, or by applying Kirchhoff's method to a flat target. As it was shown, significant differences are to expect if the beam energy is low and/or the target inclination angle is large (i.e. in the case of near grazing incidence). However, these are not the cases under investigation here, and therefore the application



ISBN 978-3-95450-141-0

of the simplified pseudo photon method is justified for the subsequent discussion.

In the following sections, different methods to separate the field Eq. (8) from the particle in the ultra–relativistic limit are introduced, and the application of these radiation sources is discussed in view of beam diagnostics.

## OPTICAL TRANSITION RADIATION

If a charged particle passes the boundary between two media with different dielectric constants, a broad band electromagnetic radiation is produced which is named transition radiation. For beam diagnostic purposes the visible part of the radiation (Optical Transition Radiation, OTR) is used and an observation geometry in backward direction is mainly chosen such that the screen has an inclination angle of 45° with respect to the beam axis, and observation is performed under 90°. In a typical monitor setup the beam is imaged via OTR using standard lens optics, and the recorded intensity profile is a measure of the particle beam spot. OTR has the advantage that it allows a fast single shot beam profile measurements, and the radiation output scales linearly with the bunch intensity (neglecting coherent effects).

In the case of OTR, the separation mechanism corresponds to the direct reflection of pseudo photons at the screen surface which acts as a mirror and which is assumed to be a perfect conductor for simplicity (otherwise the Fresnel coefficients have to be taken into account). In this reflection process, the virtual photons absorb momentum from the screen and are released from the charged particle, transformed into real photons (radiation) which can be measured at large distances as OTR. The reflection does not modify the field properties, therefore the incoming virtual and outgoing real photons are described by Eq. (8) and consequently have the same angular distribution Eq. (10).

An interesting point which goes beyond the scope of this paper is that the surrounding field of the stripped electron, moving with constant velocity inside the screen material, will be reconstructed. This reconstruction does not happen immediately and results in interesting effects, affecting e.g. the ionization loss as discussed in Ref. [29]

For a discussion about OTR based beam imaging in view of the PSF calculation, the formalism derived in the section about image formation has to be applied to the OTR field Eq. (8) in the ultra–relativistic limit, i.e neglecting the longitudinal component. Before doing so, two aspects have to be considered: (i) In the propagation integral Eq. (2), the integration has to be performed over the source plane. Particular care has to be payed concerning the integration limits, the geometrical screen dimensions and the radial field extension according to Eq. (9) have to be balanced between each other. This is especially important for high beam energies and wavelengths in the THz region where the radiation properties may be dominated by the screen boundaries. (ii) Assuming that the field contributing to the imaging process is originating from an area in the source plane which is given by the finite extension of the pseudo photon disc. With this area, an upper limit for the contribution of the quadratic phase factor in Eq. (2) can be given, i.e. for which cases this factor has to be taken into account or not. For this purpose, the spatial coordinates in that phase term which indicates the near field (Fresnel) diffraction are replaced by the source extension from Eq. (9), i.e.the phase is rewritten in the form

$$\exp\left(i\frac{k}{2a}[x_s^2+y_s^2]\right)=\exp\left(i\frac{k}{2a}\rho_{ext}^2\right)=\exp\left(i\pi\frac{\gamma^2\lambda}{a}\right)\ .$$

The quadratic phase term has to be taken into account if $a \leq \gamma^2\lambda$, which is nothing else than the range estimation for the pre–wave zone [30]. On the other hand the contribution can be omitted in the case $a \gg \gamma^2\lambda$, resulting in the wave zone condition. Therefore special care has to be taken at ultra–relativistic beam energies.

The OTR PSF is calculated based on the propagation of the pseudo photon field through the optical system Fig. 1. Details about this calculation can be found in Refs. [31]– [35] for different cases and examples. For observation in the wave zone and with the assumption for the angular acceptance of the optical system $\theta_m \gg \gamma^{-1}$, the PSF can be written as

$$\begin{aligned} I_{PSF} &\sim \zeta^{-2}\left[\zeta/\gamma\,\mathrm{K}_1(\zeta/\gamma)-\mathrm{J}_0(\zeta\theta_m)\right]^2 \\ &\sim \zeta^{-2}\left[1-\mathrm{J}_0(\zeta\theta_m)\right]^2 \end{aligned} \qquad (11)$$

with $\zeta = 2\pi R_i/(M\lambda)$, $R_i$ being the space coordinate in the image plane, $\lambda$ the wavelength of observation and $M$ the magnification of the optical system. The second equations holds in the ultra–relativistic limit, and it is interesting to note that the OTR imaging properties are independent of the beam energy in this limit.

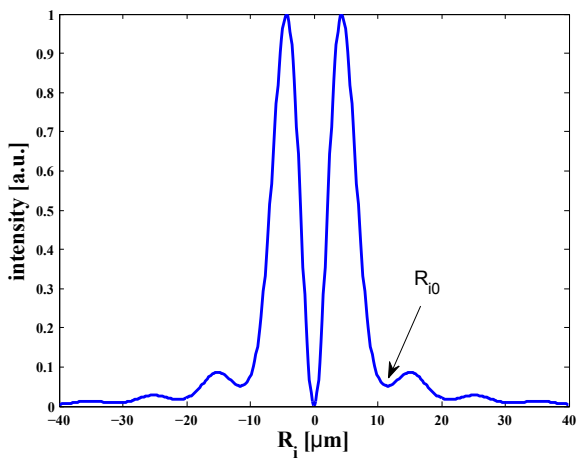


Figure 4: Calculated OTR PSF for a 855 MeV electron beam and observation with a 2" lens diameter at $\lambda$ = 500 nm, assuming 1:1 imaging.

Figure 4 shows a calculated PSF according to Eq. (11). As can be seen, the PSF exhibits an interference structure similar to the Airy disc with a central minimum, indicating the origin from a pseudo photon field. Similar to the classical resolution definition for the Airy disc, it is possible to express

ISBN 978-3-95450-141-0

the OTR resolution $R_{i0}$ as the first non–central minimum of the PSF as shown in Fig. 4, resulting in

$$R_{i0} = 1.12\frac{M\lambda}{\theta_m} \ . \qquad (12)$$

In comparison to SR where the resolution in vertical direction is limited by the angular distribution, in the case of OTR the angle $\theta_m$ is defined by the optical system because the OTR angular distribution contains sufficient intensity at larger angles. It is interesting to compare the OTR resolution with the one of a classical point source from Eq. (1). As can be seen, the latter is about a factor of two better than the one of OTR. Therefore care has to be taken while speaking about the resolution of an OTR monitor, it is not only the optical system resolution.

Transverse beam profile imaging in electron linacs is widely based on OTR as standard technique [36]. While this type of monitor prevails in electron machines covering an energy range from 10 keV [37] up to 30 GeV [38], it was also applied in proton accelerators [39, 40] and for heavy ion beam diagnostics [41]. Recent advances in OTR based beam diagnostics are summarized in Ref. [42].

Unfortunately there are physical limitations that make the method ineffective for reliable diagnostics in modern accelerators. Microbunching instabilities in high–brightness electron beams of modern linac–driven free–electron lasers (FELs) can lead to coherence effects in the emission of OTR, thus rendering it impossible to obtain a direct image of the particle beam and compromising the use of OTR monitors as reliable diagnostics for transverse beam profiles. The observation of coherent OTR (COTR) has been reported in the meantime by several facilities [43, 44]. While the use of inorganic scintillators is an alternative scheme to overcome this limitation [45], beam profile imaging with transition radiation in the EUV region is an interesting concept because it results additionally in a better resolution due to the smaller wavelength. A first proof–of–principle experiment measuring at a wavelength of $\lambda = 19.6$ nm was reported in Ref. [46].

An interesting option to measure sub–micron beam sizes with OTR is the application of PSF dominated imaging.

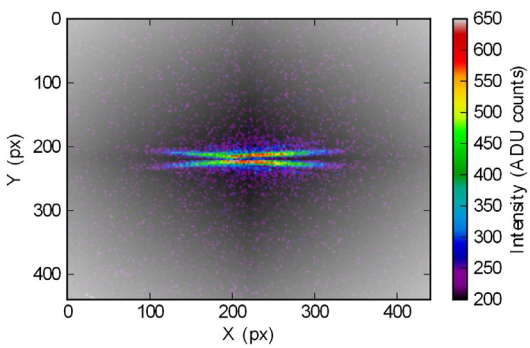


Figure 5: PSF dominated OTR beam image taken with a linear polarizer and a (550±20) nm optical filter. Image courtesy P. Karataev (RHUL), see also Ref. [47]

While in standard imaging one strives to minimize the PSF contribution such that the image is a true replica of the object, in PSF dominated imaging the object size is much smaller that the PSF, and the image is dominated by the PSF properties. In the case of OTR, a non–zero beam size results in a smearing out of the central PSF minimum, and the beam size is determined from the image contrast. The first proof–of–principle experiment was reported in Ref. [48], in the meantime the authors succeeded in measuring a minimum beam size of (0.754 ± 0.034) µm with this method [47], see also Fig. 5.

## OPTICAL DIFFRACTION RADIATION

OTR beam size diagnostics has the disadvantage that it requires the interaction of the beam with the screen. However, due to the high power density of modern high brightness beams, the energy deposition in the screen may lead to a damage of the device. Therefore the development of non–intercepting methods is essential. In this context Optical Diffraction Radiation (ODR) is an interesting candidate. This kind of radiation is generated if a charged particle beam passes close to a diffracting structure like an edge or a slit, and the physics of DR is well known in the literature, see e.g. Refs. [1, 49] and the references therein. In the subsequent discussion and similar to OTR, only backward emitted ODR will be considered because it is more convenient for beam diagnostic applications.

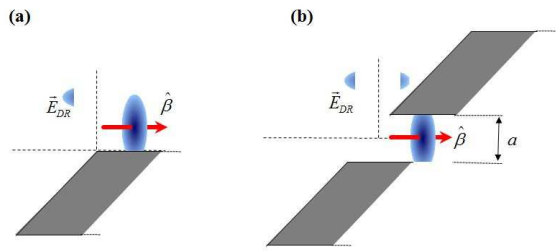


Figure 6: An ultra–relativistic electron with typical pancake field distribution passes close to (a) a metallic edge or (b) a slit in a metallic screen. Parts of the field are diffracted away and can be measured as radiation.

The mechanism of radiation generation is similar to the one of OTR and sketched in Fig. 6. But in the case of ODR it is not the complete pseudo photon field which is diffracted away, only a part of it is released from the electron. Therefore the ODR intensity will be lower than the one of OTR. Keeping in mind the radial field extension Eq. (9), it is obvious that the distance from the electron to the edge resp. the slit size $a$ in Fig. 6 should be within the range of $\rho_{ext}$ in order to efficiently generate ODR. Furthermore, in the limit $a \ll \rho_{ext}$ there is no difference between ODR and OTR.

In principle ODR can be generated at any kind of aperture. However, the use of rectangular slit shapes is advantageous because the mathematical description is simplified due to the translational invariance with respect to one coordinate, and the slit size itself can be considered as infinitely long



ISBN 978-3-95450-141-0

with respect to $\rho_{ext}$. As consequence, the beam size in only one dimension can be deduced from an ODR measurement.

For the PSF calculation of ODR based imaging, the formalism introduced before and described in the case of OTR has to be applied, taking into account the finite integration limits imposed by the slit dimensions in the source plane. Theoretical investigations about ODR imaging from a slit and a single edge are described in Refs. [32, 50]. It is intuitively clear that if only a part of the pseudo photon field is released, as it is the case in ODR, it is not the full beam image which is generated because the PSF contains information only in the region where the screen acts as a mirror, cf. the discussion in Ref. [50]. Nevertheless it is possible to deduce information about the beam size in the direction parallel to the slit edge (in the following the horizontal or $x$ direction) under the assumption that the beam has a Gaussian shape and that the distance between edge and beam axis is known. In Refs. [51, 52] relative horizontal beam sizes were measured by cross–calibrating the projected ODR image intensities with previously measured OTR ones.

In order to deduce beam size information, instead of using the ODR image the angular distribution from a slit can also be exploited. In this case, the coordinate corresponding to the direction of the displacement of the beam from the slit edge is of relevance (in the following the vertical or $y$ coordinate). Information about the beam size can be extracted from a measurement of the visibility, i.e. the ratio between the maximum intensity and the intensity in the central minimum which is smeared out due to the non–zero beam size $\sigma_y$. However, the ODR angular distribution is not only influenced by the beam size, but also by the beam offset from the slit center and by the beam divergence. While the beam offset can be controlled by a complementary diagnostic device as for example a BPM, the divergence has to be determined independently. Different schemes are proposed as discussed e.g. in Refs. [53, 54]. In order to overcome this ambiguity, in the pioneering experiment [55] a beam with very low divergence was used such that only the additional position dependence had to be taken into account which could be controlled by independent beam position measurements. With this method the authors measured beam sizes down to about 10 µm [56].

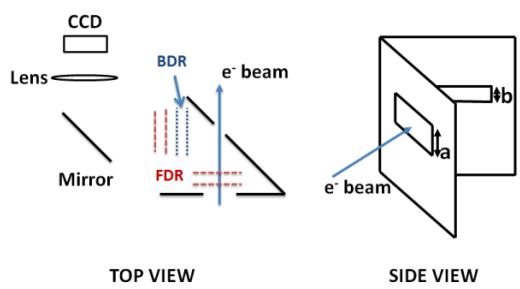


Figure 7: Setup of the ODRI experiment, explanation see text. Image courtesy A. Cianchi (INFN and Univ. Rome), see also Ref. [60].

Interferometric measurements are suitable methods to study beam divergences. ODR as well as ODTR interferometers are proposed and already in use, c.f. Refs. [57, 58]. However, this report is restricted to the application of beam profile measurements, but there is one interferometric technique to measure also beam sizes $\sigma_y$. In the Optical Diffraction Radiation Interference (ODRI) setup [59] a system of two slits with different widths is used, c.f. Fig. 7. The Forward Diffraction Radiation (FDR) from the first slit which acts additionally as a shielding mask against SR background interferes with the Backward Diffraction Radiation (BDR) from the second slit. The choice of the different slit widths allows to place the second slit within the formation length of the first one without nearly complete cancellation of the interference, thus resulting in a very compact target setup. Furthermore, the slit centers are slightly off–centered, introducing a small asymmetry in the interference pattern which helps to resolve the ambiguities. Using a complex fit routine, the contributions from beam size, beam divergence and offset can be disentangled. Figure 8 shows an example of an ODRI angular distribution measurement together with the fit to the data, demonstrating the high quality of the method. In a recent publication [60], vertical beam sizes measured with the ODRI method and with conventional OTR imaging were compared from a quadrupole scan, resulting in a very good agreement in both beam sizes and deduced vertical emittance.

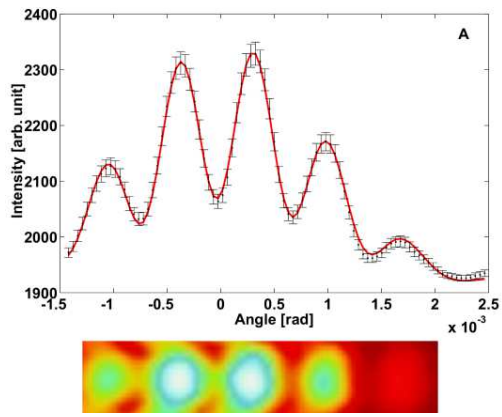


Figure 8: Top: Angular distribution of ODRI radiation with superimposed fit. Bottom: 2D angular distribution raw data. Image courtesy A. Cianchi (INFN and Univ. Rome), see also Ref. [60].

## PARAMETRIC X–RAY RADIATION

Parametric X–Ray Radiation (PXR) is emitted when a relativistic charged particle beam crosses a crystal, and the radiation process can be understood as diffraction of the virtual photon field associated with the particles at the crystallographic planes. As result, radiation is emitted in the vicinity of directions satisfying the Bragg condition. Because of the discrete momentum transfer from the crystal planes which is characterized by the reciprocal lattice vector

ISBN 978-3-95450-141-0

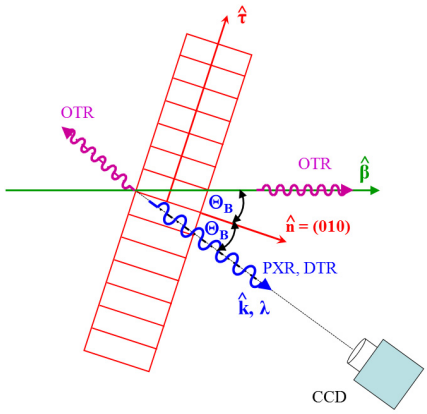


Figure 9: Sketch of the PXR geometry.

$\vec{\tau}_{hkl}$, PXR exhibits a line spectrum. The energy of the PXR lines is determined by the momentum conservation

$$\vec{p}_i = \vec{p}_f + \hbar\vec{\tau}_{hkl} + \hbar\vec{k} \tag{13}$$

with $\vec{p}_{i,f}$ the electron momentum in the initial and final state and $\hbar\vec{k}$ the associated photon momentum. Keeping in mind that the electron energy loss is given by the momentum difference projection onto the electron velocity $\delta E = (\vec{p}_i - \vec{p}_f) \cdot \vec{v}$, and that the energy loss is transferred to the emitted photons, i.e. $\delta E = \hbar\omega_{hkl}$, the energy of the PXR lines is derived as

$$\hbar\omega_{hkl} = \hbar c \frac{|\vec{\beta} \cdot \vec{\tau}_{hkl}|}{1 - \sqrt{\varepsilon}\,\vec{\beta} \cdot \hat{k}} \tag{14}$$

with $\vec{\beta} = \vec{v}/c$ the vector of the reduced electron velocity and $\varepsilon$ the crystal dielectric constant which is in the order of 1 for X–rays, see also Fig. 9. PXR is originating from a Bragg diffraction of pseudo photons, therefore their angular distribution exhibits properties of these virtual photons, i.e. it has a double–lobe structure with a characteristic opening angle of

$$\Delta\theta = \sqrt{\left(\frac{1}{\gamma}\right)^2 + \left(\frac{\hbar\omega_p}{\hbar\omega}\right)^2} \tag{15}$$

together with the characteristic central minimum. The width of this structure is larger because the radiation is generated inside the crystal, therefore material properties influence the characteristics which is indicated by the plasma frequency $\omega_p$.

PXR for beam diagnostics was independently proposed in Refs. [61, 62]. Besides the smaller radiation wavelength and the better resolution, the usage of PXR is advantageous because it is emitted from crystallographic planes inside the radiator which usually have a certain inclination angle with respect to the crystal surface, thus allowing a spatial separation from a possible COTR background which is directly generated at the surface. Disadvantage is the PXR radiation yield which is typically 1 – 2 orders of magnitude smaller than the one from transition radiation. Different schemes were proposed by the different authors: (i) imaging with an appropriate X–ray optics, (ii) bringing either the detector itself close to the target, or a scintillator converting X-rays into visible light which can be read out by a conventional CCD, and (iii) exploiting the properties of the angular distribution.

In Ref. [63] the successful imaging with an X–ray pinhole camera was reported. However, the exposure time of the detector (image plate) was 3.5 hours corresponding to an integration of 12600 beam shots. The previously reported measurement [62] to bring the image plate close to the emission point suffered from the large background contributions. In the experiment reported in [64] a scintillator was placed close to the target, but even no beam image could be observed because of the low intensity. In the same experiment the angular PXR distribution was investigated in view of sensitivity on the beam size. The measured angular distributions showed a dependency on the electron beam size, thus in principle allowing to extract information about the transverse beam profile. A preliminary analysis of these distributions indicated that not only PXR was emitted from the crystal, but in addition radiation components with narrower opening angles significantly contributed to the measured intensities. These additional radiation contributions can be interpreted as higher–order diffracted PXR, Diffracted Bremsstrahlung, or Diffracted Transition Radiation originating from the crystal entrance surface and also Bragg reflected by the crystallographic planes. As consequence additional studies are required to investigate the applicability of PXR for beam profile diagnostics.

## SMITH-PURCELL RADIATION

Smith–Purcell radiation (SPR) is emitted when an electron beam passes a diffraction grating at a fixed distance close to its surface, and the radiation mechanism can be understood as diffraction of the incoming pseudo photon field at the grating structure. The grating with spacing $D$ represents a one–dimensional Bravais structure, thus offering a discrete momentum $\hbar n\frac{D}{2\pi}$. Similar to PXR, the momentum conservation can be exploited leading to the SRP dispersion relation

$$n\lambda = D(\beta^{-1} - \cos\theta) \tag{16}$$

with n the diffraction order and $\theta$ the observation angle as measured between grating surface and outgoing photon, c.f. Fig. 10.

This dispersion relation is a necessary condition for SPR identification, but it is not sufficient because it describes

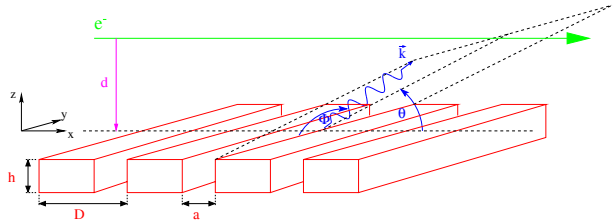


Figure 10: Sketch of the SPR geometry.



ISBN 978-3-95450-141-0

only the relative phase difference between an electron and an emitted photon. Keeping in mind that the beam passes the grating at a certain distance $d$, it is the pseudo photon field extension which uniquely determines this radiation source. While the fields scale by Eq. (9), the intensity scales with the square of the fields resulting in a characteristic decay constant $h_{int} = \frac{\lambda\beta\gamma}{4\pi}$. In Ref. [65] it is demonstrated how these SPR characteristics can be used to discriminate against background radiation.

A general overview about SPR in view of particle beam diagnostics is given in [66]. An SPR based transverse beam profile measurement is described in this reference, but as a one–dimensional scanning method it was never intended and designed to be used for this purpose, therefore it may never compete with other radiation based profile measurements described before. Furthermore, in Ref. [67] the use of SPR as a high–resolution position sensor for ultra relativistic electron beams was proposed, but the most promising application seems to be for longitudinal profile diagnostics as described in the next section.

## COHERENT RADIATION DIAGNOSTICS

A method widely applied for bunch length diagnostics is Coherent Radiation Diagnostics (CRD) [68]. Radiation is emitted coherently if the wavelength is in the order of the bunch length, i.e. information about bunch length and shape is encoded in the emission spectrum which is exploited in CRD. In case of coherent emission, the spectral intensity is strongly amplified which can be expressed in the following form:

$$\frac{\mathrm{d}U}{\mathrm{d}\lambda} = \left(\frac{\mathrm{d}U}{\mathrm{d}\lambda}\right)_1 \left(N + N(N-1)|F(\lambda)|^2\right) \qquad (17)$$

$$\text{with } F(\lambda) = \int_{-\infty}^{\infty} \mathrm{d}z\, S(z)\, e^{-2\pi i z/\lambda}.$$

Here $(\mathrm{d}U/\mathrm{d}\lambda)_1$ is the single particle emission spectrum, $N$ the number of particles in the bunch, and $F(\lambda)$ the bunch form factor which is related to the normalized bunch profile $S(z)$ via a Fourier transform. According to Eq. (17), from a measurement of the spectral intensity and with knowledge of the single electron spectrum together with the bunch charge, the form factor can be determined. Inverting the Fourier transform results in the reconstructed bunch profile $S(z)$. The situation is more complex because it is the magnitude $|F(\lambda)|$ of the form factor which is determined rather than the complex form factor itself. Reconstruction is possible only if both amplitude and phase are available. Although a strict solution of this phase–reconstruction problem is not possible, a so–called minimal phase can be constructed with the Kramers–Kronig relation which gives a handle to solve this problem satisfactory. A detailed treatment of this problem can be found e.g. in Ref. [69].

In principle any kind of coherent radiation can be used as a radiation source. Measurements were performed with coherent synchrotron radiation, transition radiation, and diffraction radiation. The resolution of CRD is limited to about 100 fs, mainly caused because of uncertainties in the spectral reconstruction. Drawback of CRD is that the radiation sources are polychromatic, i.e. a spectrometer is required for the spectral decomposition which is usually a scanning device and does not allow single–shot measurements. In this context the development of multi–stage spectrometers (see e.g. Ref. [70]) is a very interesting alternative.

SPR is an other promising alternative because the radiation source is dispersive by itself. The idea to use this kind of radiation for CRD was discussed several years ago [71, 72]. In the last years, a series of experiments was published performed by a group of authors at different accelerators in an energy range from 1.8 MeV up to 28.5 GeV [73]– [76]. These experiments demonstrate the potential to use SPR in view of CRD with the possibility to perform even single shot diagnostics.

However, there is one critical point in connection with SPR based CRD which is related to the knowledge of the exact theory describing the single particle emission spectrum in Eq. (17). In Ref. [77] a comparison of the various theories is given, demonstrating that there are discrepancies of orders of magnitude in the prediction especially at higher beam energies.

## SUMMARY

In this report, some basic applications of radiation phenomena and their physical background in view of particle beam diagnostics are presented. While some of these radiation mechanisms like SR and OTR became already a standard method for beam profile monitors, ODR for transverse and SPR for longitudinal measurements are already applied but not yet established. The application of PXR is rather new in this field, but nevertheless a stimulating phase of experiments is expected during the next years.

## ACKNOWLEDGMENT

The author acknowledges stimulating discussions and help in the preparation of this report to A.P. Potylitsyn (TPU), A. Cianchi (INFN and Univ. Rome), P. Karataev (RHUL), D. Nölle, N.A. Potylitsina–Kube and K. Wittenburg (DESY).

## REFERENCES

[1] M.L. Ter–Mikaelian, *High–Energy Electromagnetic Processes in Condensed Media*, Wiley–Interrscience, New York (1972).

[2] A. I. Akhiezer and N.F. Shul'ga, *High–Energy Electrodynamics in Matter*, Gordon and Breach Publishers, Amsterdam (1996).

[3] P. Rullhusen, X. Artru, P. Dhez, *Novel Radiation Sources using relativistic Electrons*, World Scientific, Singapore (1998).

[4] A.P. Potylitsyn, *Electromagnetic Radiation of Electrons in Periodic Structures*, Springer Tracts in Modern Physics 243, Berlin Heidelberg (2011).

[5] Radiation from Relativistic Electrons in Periodic Structures, `http://rreps.tpu.ru/`

ISBN 978-3-95450-141-0

[6] A.H. Lumpkin, Proc. BIW'12, Newport News, April 2012, TUBP02 (2012).

[7] C.F. von Weizsäcker, Z. Phys. 88 (1934) 612.

[8] E. J. Williams, Phys. Rev. 45 (1934) 729.

[9] E. Hecht, *Optics*, 2nd ed., Addison–Wesley, Reading, Massachusetts (1990).

[10] J.W. Goodman, *Introduction to Fourier Optics*, 3rd ed., Roberts & Company Publishers, Colorado (2004).

[11] B. Walasek–Höhne and G. Kube, Proc. DIPAC'11, Hamburg, May 2011, WEOB01 (2011).

[12] A. Hofmann, *The Physics of Synchrotron Radiation*, Cambridge University Press, Cambridge 2004.

[13] A. Hofmann and F. Méot, Nucl. Instr. and Meth. 203 (1982) 483.

[14] Å. Andersson and J. Tagger, Nucl. Instr. and Meth. A 364 (1995) 4.

[15] G. Kube *et al.*, Proc. BIW'04, Knoxville, May 2004, AIP Conf. Proc. 732 (2004) p.350.

[16] O. Chubar, Rev. Sci. Instrum. 66 (1995) 1872.

[17] O. Chubar and P. Elleaume, Proceedings of the EPAC'98, Stockholm, June 1998, (1998) p.1177.

[18] T. Tanaka and H. Kitamura, J. Synchrotron Rad. 8 (2001) 1221.

[19] R.A. Bosch, Nucl. Instr. and Meth. A 431 (1999) 320.

[20] O. Chubar *et al.*, Nucl. Instr. and Meth. A 435 (1999) 495.

[21] G. Geloni *et al.*, *Paraxial Green's functions in Synchrotron Radiation theory*, DESY 05-032, ISSN 0418-9833 (2005).

[22] G. Kube, Proc. DIPAC'07, Venice, May 2007, MOO1A03 (2007).

[23] C. Thomas *et al.*, Phys. Rev. ST Accel. Beams 13 (2010) 022805.

[24] T. Mitsuhashi, Proc. of BIW'04, Knoxville, May 2004, AIP Conf. Proc. 732 (2004) p.3.

[25] V. Schlott *et al.*, Proc. IBIC'13, Oxford, September 2013, TUPF09 (2013).

[26] J.W. Flanagan *et al.*, Proc. DIPAC'11, Hamburg, May 2011, WEOB03 (2011).

[27] A.G. Shkvarunets and R.B. Fiorito, Phys. Rev. ST Accel. Beams 11 (2008) 012801.

[28] D.V. Karlovets and A.P. Potylitsyn, Nucl. Instr. and Meth. B 266 (2008) 3738.

[29] N.F. Shul'ga and S.V. Trofymenko, Phys. Lett. A 376 (2012) 3572.

[30] V.A. Verzilov, Phys. Lett. A 273 (2000) 135.

[31] M. Castellano and V.A. Verzilov, Phys. Rev. ST Accel. Beams 1 (1998) 062801.

[32] A.P. Potylitsyn, Proc. NATO Workshop *Advanced Radiation Sources and Applications*, Nor-Hamberd, Springer, New York (2006), p.149.

[33] D. Xiang and W.-H. Huang, Nucl. Instr. and Meth. A 570 (2007) 357.

[34] G. Kube, *Imaging with Optical Transition Radiation, Transverse Beam Diagnostics for the XFEL*, TESLA-FEL Report 2008-01 (2008).

[35] G. Stupakov, *Image Formation by Incoherent and Coherent Transition Radiation from Flat and Rough Surfaces*, SLAC-PUB-14758 (2011).

[36] R.B. Fiorito and D.W. Rule, Proc. BIW'93, Sante Fe, October 1993, AIP Conf. Proc. 319 (1994) p.21.

[37] R.B. Fiorito *et al.*, Proc. PAC'07, Albuquerque, June 2007, FRPMS033 (2007).

[38] P. Catravas *et al.*, Proc. PAC'99, New York, March/April 1999, (1999) p.2111.

[39] O.V. Afanasyev *et al.*, Proc. BIW'06, Batavia, May 2006, AIP Conf. Proc. 868 (2006) p.534.

[40] V.E. Scarpine *et al.*, Proc. BIW'06, Batavia, May 2006, AIP Conf. Proc. 868 (2006) p.473.

[41] B. Walasek-Höhne *et al.*, Proc. HB 2012, Beijing, China, September 2012, THO3C01 (2012).

[42] R.B. Fiorito, Proc. PAC'09, Vancouver (BC), May 2009, TU3GRI02 (2009).

[43] H. Loos *et al.*, Proc. FEL'08, Gyeongju, August 2008, THBAU01 (2008).

[44] S. Wesch and B. Schmidt, Proc. DIPAC'11, Hamburg, May 2011, WEOA01 (2011).

[45] G. Kube *et al.*, Proc. IPAC'12, New Orleans, May 2012, WEOAA02 (2012).

[46] L.G. Sukhikh *et al.*, Proc. IPAC'12, New Orleans, May 2012, MOPPR019 (2012) and submitted to Phys. Rev. ST Accel. Beams.

[47] K. Kruchinin *et al.*, J. Phys.: Conf. Series 517 (2014) 012011 and Proc. IBIC'13, Oxford, September 2013, WEAL2 (2013).

[48] P. Karataev *et al.*, Phys. Rev. Lett. 107 (2011) 174801.

[49] A.P. Potylitsyn, M.I. Ryazanov, M.N. Strikhanov, A.A. Tishchenko, *Diffraction Radiation from Relativistic Particles*, Springer Tracts in Modern Physics 239, Berlin Heidelberg (2010).

[50] D. Xiang *et al.*, Phys. Rev. ST Accel. Beams 10 (2007) 062801.

[51] A.H. Lumpkin *et al.*, Phys. Rev. ST Accel. Beams 10 (2007) 022802.

[52] P. Evtushenko, *et al.*, Proc. BIW'08, Tahoe City, May 2008, WECOTC01 (2008).

[53] R.B. Fiorito and D.W. Rule, Nucl. Instr. and Meth. B 173 (2001) 67.

[54] N.A. Potylitsina–Kube and X. Artru, Nucl. Instr. and Meth. B 201 (2003) 172.

[55] P. Karataev *et al.*, Phys. Rev. Lett. 93 (2004) 244802.

[56] P. Karataev *et al.*, Nucl. Instr. and Meth. B 227 (2005) 158.

[57] R.B. Fiorito *et al.*, Phys. Rev. ST Accel. Beams 9 (2006) 052802.

[58] M.A. Holloway *et al.*, Phys. Rev. ST Accel. Beams 11 (2008) 082801.

[59] A. Cianchi *et al.*, Phys. Rev. ST Accel. Beams 14 (2011) 102803.



ISBN 978-3-95450-141-0

[60] A. Cianchi *et al.*, accepted for publication in New Journal of Physics (2014).

[61] A. Gogolev, A. Potylitsyn, G. Kube, J. Phys. Conference Series 357 (2012) 012018.

[62] Y. Takabayashi, Phys. Lett. A 376 (2012) 2408.

[63] Y. Takabayashi and K. Sumitani, Phys. Lett. A 377 (2013) 2577.

[64] G. Kube *et al.*, Proc. IPAC'13, Shanghai, May 2013, MOPME011 (2013).

[65] G. Kube *et al.*, Phys. Rev. E 65 (2002) 056501.

[66] G. Kube, Proc. DIPAC'03, Mainz, May 2003, IT09 (2003).

[67] G. Doucas *et al.*, Nucl. Instr. and Meth. A 474 (2001) 10.

[68] O. Grimm, Proc. PAC'07, Albuquerque, June 2007, THYC02 (2007).

[69] O. Grimm and P. Schmüser, TESLA-FEL Report 2006-03 (2006).

[70] S. Wesch *et al.*, Nucl. Instr. and Meth. A 665 (2011) 40.

[71] M.C. Lampel, Nucl. Instr. and Meth. A 385 (1997) 19.

[72] D. Nguyen, Nucl. Instr. and Meth. A 393 (1997) 514.

[73] G. Doucas *et al.*, Phys. Rev. ST Accel. Beams 5 (2001) 072802.

[74] G. Doucas *et al.*, Phys. Rev. ST Accel. Beams 9 (2006) 092801.

[75] V. Blackmore *et al.*, Phys. Rev. ST Accel. Beams 12 (2009) 032803.

[76] H.L. Andrews *et al.*, Phys. Rev. ST Accel. Beams 17 (2014) 052802.

[77] D.V. Karlovets and A.P. Potylitsyn, Phys. Rev. ST Accel. Beams 9 (2006) 080701.



ISBN 978-3-95450-141-0